

Detection of Earth's free oscillations utilizing TianQin

Yuxin Yang^{1,2}, Kun Liu², Xuefeng Zhang^{1,2*}, and Yi-Ming Hu^{1,2*}

¹MOE Key Laboratory of TianQin Mission, TianQin Research Center for Gravitational Physics, Frontiers Science Center for TianQin, Gravitational Wave Research Center of CNSA, Sun Yat-sen University (Zhuhai Campus), Zhuhai, 519082, China.

²School of Physics and Astronomy, Sun Yat-sen University (Zhuhai Campus), Zhuhai, 519082, China.

*Address correspondence to: zhangxf38@sysu.edu.cn, huyiming@sysu.edu.cn

Abstract

The measurement of Earth's free oscillations plays an important role in studying the Earth's large-scale structure. Space technology development presents a potential method to observe these normal modes by measuring inter-satellite distances. However, the disturbance from the Earth's low-degree gravity field makes it challenging for low Earth orbit gravity measurement satellites such as Gravity Recovery and Climate Experiment (GRACE) and TianQin-2 to extract signals from Earth's free oscillations directly. Here, we propose that by taking advantage of the high Earth orbit, the TianQin satellites can effectively avoid this disturbance, enabling direct measurement of Earth's free oscillations. We derive an analytical waveform to describe the response of Earth's free oscillations in TianQin. Based on this waveform, we use Bayesian analysis to extract the normal modes from numerical simulation data and perform parameter estimation. Our findings reveal that for a magnitude 7.9, Wenchuan-like earthquake, the resulting free oscillations will generate a signal that signal-to-noise ratio (SNR) is 73 in TianQin, and approximately 9 different modes can be distinguished. This result shows TianQin can open a new window to examine the Earth's free oscillations and study the Earth's interior and earthquakes independently from ground-based gravity measurement.

1 Introduction

Earth's free oscillations, also known as normal modes of the Earth, are standing waves along the surface and radius of the Earth. Similar to natural vibrations, the Earth's free oscillations occur as the planet responds to disturbances like earthquakes. The amplitudes, frequencies, and damping times of the Earth's free oscillations are governed by the intrinsic properties of the Earth. Therefore, detailed measurement of the Earth's free oscillations provides a unique window to constrain the large-scale structure of the Earth. For example, the observation of normal modes provides information to

describe the Earth's interior structure [1, 2], the inner core of Earth [3–8], and the source mechanism of earthquakes [9–11].

After the 1960 Chilean earthquake, a long-period oscillation of local gravitational acceleration was reported. The pattern closely follows the theoretical prediction of the Earth's free oscillations, and therefore it was regarded as the first observation [12, 13]. Earth's free oscillation signals were initially identified by investigating the Fourier transform of the observational data from individual gravimeters [14, 15]. In order to enhance the signal-to-noise ratio (SNR) and therefore increase the precision of estimated parameters, data stacking methods were proposed. Such methods study observation data combined from multiple gravimeters [16], including the spherical harmonic stacking (SHS) [17], the optimal sequence estimation (OSE) [18], and the multistation experiment (MSE) [19]. Technological advancements, notably the adoption of Superconducting Gravimeters, have significantly enhanced the detection precision of Earth's normal modes [20]. So far, a large number of Earth's normal modes along with their splitting spectra have been detected by ground-based stations [21–23].

The advancement of space technology presents a potential alternative data source for detecting these oscillations. The prospect of detecting Earth's normal modes by measuring inter-satellite distances was first suggested and performed by Ghobadi-Far et al. [24]. However, no such oscillation signal was reported in the observation data of the Gravity Recovery and Climate Experiment (GRACE). Its successor, the Gravity Recovery and Climate Experiment Follow-On Mission (GRACE-FO), has significantly enhanced measurement precision by three orders of magnitude[25, 26]. Yet again there was no reported oscillation signal. The proposed space gravity measurement mission, TianQin-2, also holds considerable promise for detecting Earth's normal modes [27, 28]. Satellites from these two missions operate in low Earth orbit on the order of hundreds of kilometers. As shown in FIG. 5 of [29], for low-orbit gravity measurement mission, Earth's high-order global gravity would generate a significant signal at the low-frequency band ($< 10^{-2}$ Hz). The determination precision of the low-frequency band and low-order parameters is limited by this sensitivity aliasing effect. The signals of Earth's free oscillations are normally buried under the global gravity signals. Therefore, it is difficult to observe Earth's normal modes directly, which could explain the non-observation. On the other hand, the space-borne gravitational wave (GW) detector TianQin has the potential to observe Earth's free oscillations [30]. Unlike the aforementioned missions, TianQin satellites adopt a high Earth orbit ($\sim 10^5$ km), which is more sensitive to the low-frequency band and low-order parameters. In addition, with a three-satellite six-links detection system instead of two-satellite two-links system and the high-precision inter-satellite distance measurement, TianQin will extract more information from the gravitational field.

TianQin is a space-borne GW detector with geocentric satellite orbit [27, 31]. It plans to launch three identical satellites orbiting at an altitude of $\sim 10^5$ km, forming a nearly equilateral triangle constellation. TianQin detects GWs by measuring distance changes between satellites using laser interferometry with picometer-level precision. The designed detection frequency band of TianQin is about $10^{-4} \sim 1$ Hz, covering the frequencies of prominent Earth's free oscillations [2]. In this frequency range, neither the Earth's static gravitational field nor the free oscillations background will produce a detectable signal in TianQin [32, 33]. However, major earthquakes such as the 2008

Wenchuan earthquake will leave a clear mark [30], suggesting that it is possible to identify Earth’s normal modes from TianQin data in the future.

In this work, we aim to develop data analysis tools to extract signals of Earth’s free oscillations from simulated TianQin data. For GW signals, the matched filtering method is often employed to extract signals from data [34]. This method utilizes theoretical waveform templates to correlate and match observation data. A high likelihood means the data has a strong response to the template. In Section 2.1, we introduce the basic information of TianQin mission and time-delay interferometry (TDI) method [35–37]. This method algebraically combines the signals from different arms of interferometry, which is anticipated to be used to cancel laser phase noise. In Section 2.2, we briefly introduce the Earth’s free oscillations model used in this study, as well as the numerical method for generating simulated signals in TianQin based on this model. In Section 2.3, we first derive the waveform of the Earth’s free oscillation, combined with the detector’s response in the first-generation TDI-X channels. This can be achieved by following the analysis based on the satellite-to-satellite tracking work of GRACE [24] and TianQin [33], which calculates the acceleration changes between two satellites under the influence of the Earth’s gravitational field based on Kaula’s linear perturbation approach [38, 39]. Finally, we perform a Bayesian analysis through Markov Chain Monte Carlo (MCMC) and Fisher information matrix (FIM) in Section 2.4. We summarize our results in Section 3 and show our main conclusions in Section 4.

2 Materials and Methods

2.1 TianQin mission and time-delay interferometry method

The primary scientific objective of TianQin is observing GW sources within the millihertz band, which requires extreme sensitivity [31]. The fundamental principle underlying GW detection entails the measurement of picometer-level distance variations between distinct free-fall test masses utilizing laser interferometry. To mitigate measurement noise stemming from the laser interferometer, the interferometer arms must be of equal length. Consequently, in the initial proposal, the satellite orbits of TianQin would form an equilateral triangle around the Earth, facilitating the assumption of satellites operating in quasi-circular orbits as discussed in Section 2.3. From a scientific perspective, the semi-major axis of the satellite orbits is approximately 10^5 km, and the plane of the celestial equator of the satellites points to J0806. The details of the parameters for the TianQin orbit can be found in Table 1.

The design of an equal-arm interferometer for GW detectors can mitigate measurement noise originating from the laser interferometer, particularly laser frequency fluctuation noise. Nonetheless, maintaining equal arm lengths in interferometry with sufficient precision poses a challenge for space-borne GW detectors. Tinto et al. [35] proposed the TDI method to address this issue. This method algebraically combines the signal from different arms of interferometry, constructing equivalent arms with equal lengths to eliminate laser frequency fluctuation noise. In this article, we focus on the first-generation TDI and provide the construction method of the TDI channel in the following.

Three symmetrical TDI channels denoted as X, Y, and Z, respectively, can be constructed for

Symbols	Parameters	values
a	Orbit radius	10^5 km
e	Eccentricity	0
i	Inclination	74.5°
Ω	Longitude of ascending node	211.6°
GM	Earth's gravity constant	$3.986 \times 10^{-14} \text{m}^3/\text{s}^2$
R	Average Earth radius	$6.378 \times 10^6 \text{m}$
γ	Spread angle between two satellites	120°
$1/f_e$	Earth rotation period	86164s
$1/f_o$	Satellite rotation period	314709s
ϕ_{e0}	Earth Initial phase	136.8°
ϕ_{o0}	Satellite Initial phase	30°

Table 1: The parameters designed for TianQin and setting in the analytical model.

the space-borne GW detectors with satellites orbiting in an equilateral triangular configuration like TianQin. Without loss of generality, we will only discuss the construction method for the TDI-X channel. We denote the laser phase signals observed in satellite 1 come from different arms as $\phi_1(t)$ and $\phi_{1'}(t)$, which could be written as

$$\begin{aligned}\phi_1(t) &= p(t - 2L_3/c) - p(t) + s_1^h(t) + n_1(t), \\ \phi_{1'}(t) &= p(t - 2L_2/c) - p(t) + s_{1'}^h(t) + n_{1'}(t),\end{aligned}\tag{1}$$

where $p(t)$ represents the laser frequency noise, L_i denotes the length of different arms, c denotes the speed of light, $s_i^h(t)$ are the GW signals and $n_i(t)$ represents other noise. Obviously, when the length of different arms is unequal (i.e., $L_2 \neq L_3$), the laser frequency noise persists if we construct the Michelson channel using $\Delta\phi(t) = \phi_1(t) - \phi_{1'}(t)$, as typically done with a laser interferometer. Therefore, we propose defining the TDI-X channel as

$$\phi_X(t) = \phi_1(t) - \phi_{1'}(t) - [\phi_1(t - 2L_2/c) - \phi_{1'}(t - 2L_3/c)].\tag{2}$$

We introduce the Time-Delay operator

$$\mathcal{D}_i \phi(t) \equiv \phi(t - L_i/c),\tag{3}$$

which satisfies

$$\mathcal{D}_i \mathcal{D}_j \phi(t) = \phi(t - L_i/c - L_j/c) = \mathcal{D}_j \mathcal{D}_i \phi(t).\tag{4}$$

Keeping only the laser frequency noise, the data in the TDI-X channel could be written as

$$\begin{aligned}\phi_X(t) &= \phi_1(t) - \phi_{1'}(t) - [\phi_1(t - 2L_2/c) - \phi_{1'}(t - 2L_3/c)] \\ &= (1 - \mathcal{D}_2^2) \phi_1(t) - (1 - \mathcal{D}_3^2) \phi_{1'}(t) \\ &= [(1 - \mathcal{D}_2^2)(\mathcal{D}_3^2 - 1) - (1 - \mathcal{D}_3^2)(\mathcal{D}_3^2 - 1)] p(t) \\ &= 0,\end{aligned}\tag{5}$$

which proves that the TDI method could cancel the laser frequency noise. Utilizing the same method, the TDI-Y and TDI-Z channel, observed in satellites 2 and 3, respectively, could be defined as

$$\phi_Y(t) = \phi_2(t) - \phi_{2'}(t) - [\phi_2(t - 2L_3/c) - \phi_{2'}(t - 2L_1/c)], \quad (6)$$

$$\phi_Z(t) = \phi_3(t) - \phi_{3'}(t) - [\phi_3(t - 2L_1/c) - \phi_{3'}(t - 2L_2/c)]. \quad (7)$$

Another widely used TDI channel, AET channel [36], can be defined as linear combinations of XYZ channel:

$$A = \frac{1}{\sqrt{2}}(Z - X), \quad (8)$$

$$E = \frac{1}{\sqrt{6}}(X - 2Y + Z), \quad (9)$$

$$T = \frac{1}{\sqrt{3}}(X + Y + Z). \quad (10)$$

This kind of channel consists of three orthogonal channels, making noise uncorrelated in different channels. A and E channels still contain GW signals, while GW response is very weak in the T channel. Therefore, the T channel is usually used to monitor noise in GW detection. The following derivation will focus on the Earth's free oscillations' signals in the TDI-X channel. It's easy to generalize our method to the response on the other channels.

2.2 Earth's free oscillations model and numerical simulation

The Earth's free oscillations are categorized into spheroidal and toroidal modes [40]. Toroidal modes do not induce radial deformation or alter the Earth's gravitational field. Conversely, spheroidal modes encompass both radial and horizontal movements, resulting in alterations to the Earth's gravitational field. Only the latter can perturb satellite orbits, rendering them detectable by Tian-Qin. Herein, we exclusively focus on the spheroidal modes incited by the major earthquake.

An earthquake is commonly characterized using the point-source double-couple model along with pertinent parameters including scalar seismic moment, dip, rake, and strike [41]. The amplitudes of the Earth's free oscillations, which are induced by seismic events, are determined by these earthquake parameters. The normal modes of Earth can be derived through computation utilizing the Preliminary Reference Earth Model (PREM), a widely adopted nonrotating, elastic, spherically symmetric, one-dimensional Earth model [2]. Transforming seismic parameters into Earth's free oscillation parameters can be achieved by spherical harmonic decomposition and coordinate transformation [41–43]. Finally, the perturbation in gravity resulting from free oscillations is expressed through a series of coefficients denoted as ${}_l\Delta\bar{C}_{nm}$ and ${}_l\Delta\bar{S}_{nm}$.

Then we introduce the details of these parameters describing the variations in Earth's gravitational field. Within the framework of the International Terrestrial Reference System (ITRS), a satellite that is located at spherical coordinates radius r , co-latitude θ , and longitude λ will experi-

ence the Earth's gravity field described as

$$V(r, \theta, \lambda) = \frac{GM}{R} \sum_{n=0}^N \sum_{m=0}^n \left(\frac{R}{r}\right)^{n+1} \times (\bar{C}_{nm} \cos(m\lambda) + \bar{S}_{mn} \sin(m\lambda)) \bar{P}_{nm}(\cos \theta), \quad (11)$$

where G is the gravitational constant, M is the Earth's total mass, R is the Earth's average radius, n and m correspond to the degree and order of spherical harmonic expansion, respectively [44]. The symbol N denotes the truncation degree of the spherical harmonics function.

Eq. (11) delineates a scenario wherein the gravitational field remains temporally invariant. Upon the occurrence of a significant earthquake, resulting in the generation of Earth's free oscillations, the coefficients \bar{C}_{nm} and \bar{S}_{mn} cease to remain constant. The fluctuations in the Earth's gravitational field can be modeled as [24, 45]

$$\begin{cases} \bar{C}_{nm}(t) = \bar{C}_{nm} + \sum_{l=0}^L l \Delta \bar{C}_{nm} l \xi_n(t - t_0), \\ \bar{S}_{nm}(t) = \bar{S}_{nm} + \sum_{l=0}^L l \Delta \bar{S}_{nm} l \xi_n(t - t_0), \end{cases} \quad (12)$$

where l marks free oscillation overtones, L represents the maximum overtone, and t_0 denotes the time of earthquake occurrence. The coefficients $l \Delta \bar{C}_{nm}$ and $l \Delta \bar{S}_{nm}$ describe the magnitudes of free oscillation across various spherical harmonics. The time-dependent functions are defined as

$$l \xi_n(t) = \begin{cases} 0, & t < 0 \\ 1 - l \tau_n(t) \cos(2\pi_l f_n t), & t \geq 0 \end{cases} \quad (13)$$

where

$$l \tau_n(t) = \exp\left(-\frac{2\pi_l f_n (t - t_0)}{2_l Q_n}\right). \quad (14)$$

For each degree and overtones, $l f_n$ represents the frequency of oscillations, while $l Q_n$ denotes the attenuation factor characterizing the decay rate of free oscillations. The frequency and attenuation factor of each oscillation overtone can be computed utilizing PREM.

Based on the Earth's free oscillations model, a simulation of observation data can be produced by numerical method. In this work, we use the orbit evolution simulation program **TQPOP** [32] to generate satellites' positions numerically. Then, we calculate the laser propagation time between satellites to produce the observation data in single links, which are subsequently transformed into TDI channel data.

However, the numerical method requires a long computation time, making the use of this waveform for signal extraction difficult. Therefore, in this work, we propose an analytical waveform for signal extraction. This waveform is derived based on a simplified model that assumes the TianQin satellites operate in quasi-circular orbit, with the same orbital altitude, and forms an equilateral triangle constellation. It can describe the response of Earth's free oscillation in the first-generation TDI-X channel. The details of the waveform derivation will be presented in Section 2.3.

2.3 Analytical model derivation

This section aims to derive an analytical formula to describe the response of Earth's free oscillations. The Earth's normal modes could be modeled by the Eq. (11) - Eq. (14).

Firstly, we deduce the movement of satellites under the Earth's gravity field. In the International Celestial Reference System (ICRS), the gravitational potential experienced by satellites due to Earth can be expressed as

$$V(a, i, e, \omega, M, \Omega, \Theta) = \frac{GM}{R} \sum_{n=0}^N \left(\frac{R}{a} \right)^{n+1} \times \sum_{m=0}^n \sum_{p=0}^n \bar{F}_{nmp}(i) \sum_{q=-\infty}^{\infty} G_{npq}(e) S_{nmpq}(\omega, M, \Omega, \Theta), \quad (15)$$

where the arguments $\{a, i, e, \omega, M, \Omega, \Theta\}$ represent the semi-major axis, the inclination, the eccentricity, the argument of perigee, the mean anomaly, the right ascension of the ascending node, and the Greenwich Apparent Sidereal Time (GAST), respectively. The inclination function $\bar{F}_{nmp}(i)$ describes the impact of satellite orbital inclination and will be discussed extensively later [38, 39]. The function $G_{npq}(e)$ characterizes the impact of the eccentricity. However, we do not address this function in the present work, as the rationale will be explained subsequently. The function S_{nmpq} is defined as

$$S_{nmpq}(\omega, M, \Omega, \Theta) = \alpha_{nm} \cos \phi_{nmpq} + \beta_{nm} \sin \phi_{nmpq}. \quad (16)$$

The coefficients $\{\alpha_{nm}, \beta_{nm}\}$ are rearrangements of $\{\bar{C}_{nm}, \bar{S}_{nm}\}$ (Eq. 11),

$$\begin{aligned} \alpha_{nm} &= \begin{cases} \bar{C}_{nm}, & n - m = \text{even} \\ -\bar{S}_{nm}, & n - m = \text{odd} \end{cases} \\ \beta_{nm} &= \begin{cases} \bar{S}_{nm}, & n - m = \text{even} \\ \bar{C}_{nm}, & n - m = \text{odd} \end{cases} \end{aligned} \quad (17)$$

and the angular argument reads

$$\phi_{nmpq} = (n - 2p)\omega + (n - 2p + q)M + m(\Omega - \Theta). \quad (18)$$

TianQin's satellites orbit in quasi-circular paths, enabling us to assume an eccentricity of zero for the orbits. Therefore, we consider only the case where $e = 0$ for the function $G_{npq}(e)$. The function $G_{npq}(0)$ equals 1 when $q = 0$ and becomes zero for other values of q . Consequently, we can disregard this function in Eq. (15), simplifying it to [46]

$$V = \sum_{n=0}^N \sum_{m=0}^n \sum_{k=-n}^n u_n(a) \bar{F}_{mp}^k(i) (\alpha_{nm} \cos \varphi_{mk} + \beta_{nm} \sin \varphi_{mk}), \quad (19)$$

with the angular argument

$$\varphi_{mk} = k\varphi^o + m\varphi_e, \quad (20)$$

and

$$\varphi^o = \omega + M, \quad \varphi_e = \Omega - \Theta. \quad (21)$$

To be convenient, we rearrange the summation indices with $k = n - 2p$ and define

$$u_n(a) = \frac{GM}{R} \left(\frac{R}{a} \right)^{n+1}. \quad (22)$$

Then we give the expression for the inclination function

$$\begin{aligned} \bar{F}_{nm}^k(i) = & \sum_{s=0}^m \sum_{t=t_1}^{t_2} \sum_{b=b_1}^{b_2} \sqrt{(2 - \delta_{0m}) (2n + 1) \frac{(n - m)!}{(n + m)!}} \left[\frac{(-1)^{b+g}}{2^{2n-2t}} \frac{(2n - 2t)!}{t!(n - t)!(n - m - 2t)!} \right. \\ & \left. \times C_m^s C_{n-m-2t+s}^b C_{m-s}^{n-\frac{1}{2}-t-b} \sin^{n-m-2t}(i) \cos^s(i) \right] \end{aligned} \quad (23)$$

by using the auxiliary index

$$g = \begin{cases} \frac{n-m}{2}, & n - m = \text{even} \\ \frac{n-m-1}{2}, & n - m = \text{odd} \end{cases} \quad (24)$$

with

$$t_1 = 0, \quad t_2 = \begin{cases} -\frac{1}{2}k + \frac{1}{2}n, & k \geq n - 2g \\ g, & k \leq n - 2g \end{cases} \quad (25)$$

and

$$\begin{aligned} b_1 &= \begin{cases} 0, & 2s - k - 2t \leq 2m - n, \\ s - \frac{1}{2}k - t + \frac{1}{2}n - m, & 2s - k - 2t \geq 2m - n, \end{cases} \\ b_2 &= \begin{cases} s - 2t + n - m, & 2s + k - 2t \leq 2m - n, \\ -\frac{1}{2}k - t + \frac{1}{2}n, & 2s + k - 2t \geq 2m - n. \end{cases} \end{aligned} \quad (26)$$

Utilizing the formula describing the gravitational potential experienced by satellites, we can calculate the range acceleration between two TianQin satellites. Here, subscripts $\{1, 2\}$ denote two different satellites, SC1 and SC2, respectively. Subsequently, we define L as the distance between two TianQin satellites, allowing us to express the range acceleration \ddot{L} as (refer to [46] for further details)

$$\ddot{L} = \frac{1}{a} \left(\frac{\partial V_2}{\partial \varphi_2^o} - \frac{\partial V_1}{\partial \varphi_1^o} \right) \cos \left(\frac{\gamma}{2} \right) + \left(\frac{\partial V_2}{\partial r_2} + \frac{\partial V_1}{\partial r_1} \right) \sin \left(\frac{\gamma}{2} \right). \quad (27)$$

We incorporate the gravitational potential formula given by Eq. (19) into Eq. (27). Subsequently, we substitute φ^o with φ^{om} , where φ^{om} represents the argument of latitude of the midpoint between SC1 and SC2. Thus, the formula for range acceleration becomes [33]

$$\ddot{L} = \sum_{l=0}^L \sum_{n=0}^N \sum_{m=0}^n \sum_{k=-n}^n \Xi_{nmk}(a, i, \gamma) [\alpha_{nm} \cos(m\varphi_e + k\varphi^{om}) + \beta_{nm} \sin(m\varphi_e + k\varphi^{om})], \quad (28)$$

where

$$\begin{aligned}\Xi_{nmk}(a, i, \gamma) &= -2 \frac{u_n(a)}{a} \bar{F}_{nm}^k(i) \\ &\times \left[k \sin\left(k \frac{\gamma}{2}\right) \cos\left(\frac{\gamma}{2}\right) + (n+1) \sin\left(\frac{\gamma}{2}\right) \cos\left(k \frac{\gamma}{2}\right) \right].\end{aligned}\quad (29)$$

It is important to note that the formulas derived above only account for a static gravity field. In the scenario of a time-varying gravity field induced by the Earth's free oscillations, it is necessary to convert the static coefficients $\bar{C}_{nm}, \bar{S}_{mn}$ to time-varying coefficients $\bar{C}_{nm}(t), \bar{S}_{mn}(t)$ using Eq. (12). Additionally, the parameters φ^{om} and φ_e are time-varying and given by $2\pi f_o t + \phi_{o0}$ and $2\pi f_e t + \phi_{e0}$, respectively, where f_o represents the frequency of the satellites' rotation and f_e denotes the frequency of the Earth's rotation. Subsequently, we express the time-varying range acceleration as

$$\begin{aligned}\ddot{L}(t) &= \sum_{n=0}^N \sum_{m=0}^n \sum_{k=-n[2]}^n \frac{1}{2} \Xi_{nmk}(a, i, \gamma) \exp[i\lambda_n(t - t_0)] \times \\ &[-i\Delta\alpha_{nm} \cos(i\omega_{mnk}^+(t - t_0) + \phi_{mk}) + i\Delta\beta_{nm} \sin(i\omega_{mnk}^+(t - t_0) + \phi_{mk}) \\ &- i\Delta\alpha_{nm} \cos(i\omega_{mnk}^-(t - t_0) - \phi_{mk}) - i\Delta\beta_{nm} \sin(i\omega_{mnk}^-(t - t_0) - \phi_{mk})],\end{aligned}\quad (30)$$

where

$$i\lambda_n = \frac{2\pi i f_n}{2i Q_n}, \quad (31)$$

and

$$i\omega_{mnk}^+ = 2\pi (i f_n + m f_e - k f_o), \quad i\omega_{mnk}^- = 2\pi (i f_n - m f_e + k f_o). \quad (32)$$

The phase of different modes can be expressed as

$$\phi_{mk} = m\phi_{e0} - k\phi_{o0} \quad (33)$$

Upon performing two integrations, the range acceleration transforms into the differential arm length ΔL . Typically, observation data from TianQin is represented in the form of strain, denoted as $h = \Delta L/L$, where L signifies the unperturbed arm length. Thus, the observation data from a single arm, induced by Earth's free oscillations, can be formulated as follows

$$\begin{aligned}h(t) &= \sum_{l=0}^L \sum_{n=0}^N \sum_{m=0}^n \sum_{k=-n[2]}^n \frac{1}{2L} \Xi_{nmk}(a, i, \gamma) \exp(i\lambda_n(t - t_0)) \times \\ &[iL_{nmk}^{+c} \cos(i\omega_{mnk}^+(t - t_0) + \phi_{mk}) + iL_{nmk}^{+s} \sin(i\omega_{mnk}^+(t - t_0) + \phi_{mk}) \\ &+ iL_{nmk}^{-c} \cos(i\omega_{mnk}^-(t - t_0) - \phi_{mk}) + iL_{nmk}^{-s} \sin(i\omega_{mnk}^-(t - t_0) - \phi_{mk})],\end{aligned}\quad (34)$$

where

$$\begin{aligned}
{}_l L_{mnk}^{+c} &= \frac{1}{(({}_l \lambda_n)^2 + ({}_l \omega_{mnk}^+)^2)^2} (-{}_l \Delta \alpha_{nm} ({}_l \lambda_n^2 - ({}_l \omega_{mnk}^+)^2) - 2 {}_l \Delta \beta_{nm} {}_l \lambda_{nl} \omega_{mnk}^+), \\
{}_l L_{mnk}^{+s} &= \frac{1}{(({}_l \lambda_n)^2 + ({}_l \omega_{mnk}^+)^2)^2} (-{}_l \Delta \beta_{nm} ({}_l \lambda_n^2 - ({}_l \omega_{mnk}^+)^2) + 2 {}_l \Delta \alpha_{nm} {}_l \lambda_{nl} \omega_{mnk}^+), \\
{}_l L_{mnk}^{-c} &= \frac{1}{(({}_l \lambda_n)^2 + ({}_l \omega_{mnk}^-)^2)^2} (-{}_l \Delta \alpha_{nm} ({}_l \lambda_n^2 - ({}_l \omega_{mnk}^-)^2) + 2 {}_l \Delta \beta_{nm} {}_l \lambda_{nl} \omega_{mnk}^-), \\
{}_l L_{mnk}^{-s} &= \frac{1}{(({}_l \lambda_n)^2 + ({}_l \omega_{mnk}^-)^2)^2} ({}_l \Delta \beta_{nm} ({}_l \lambda_n^2 - ({}_l \omega_{mnk}^-)^2) + 2 {}_l \Delta \alpha_{nm} {}_l \lambda_{nl} \omega_{mnk}^-).
\end{aligned} \tag{35}$$

As previously mentioned, TDI is extensively employed in space-borne GW detectors. The final data acquired from TianQin is processed by TDI. It is necessary to derive the formula for the Earth's free oscillation signals after undergoing TDI processing. As demonstrated in Section 2.1, TDI fundamentally involves algebraic calculations of data from various arms. Consequently, we must consider the effects on different arms simultaneously. Eq. (33) reveals that the signal phase is dependent on both the Earth's phase and the orbit's phase. The Earth's phase is the same for all arms of TianQin, while the orbit's phase is different. Let $\phi_{mk}^{(1)}$ denote the signal phase in one arm. Then, the phase of another arm in the opposite direction of the satellites' movement can be expressed as

$$\phi_{mk}^{(2)} = \phi_{mk}^{(1)} + k\gamma. \tag{36}$$

Given the phase relationship between different arms as described by Equation (36), let $h(t, \phi_{mk})$ represent the signal in one arm, and denote the signal in another arm as $h(t, \phi_{mk} + k\gamma)$. Recall the algebraic construction of the TDI-X channel using Eq. (2). Subsequently, we utilize a linear approximation to describe the time delay effect and provide the expression of the signal in the TDI-X channel

$$\begin{aligned}
h_X(t) &= [h(t, \phi_{mk}) + h(t - \Delta t, \phi_{mk}) + h(t - 2\Delta t, \phi_{mk} + k\gamma) + h(t - 3\Delta t, \phi_{mk} + k\gamma)] \\
&\quad - [h(t, \phi_{mk} + k\gamma) + h(t - \Delta t, \phi_{mk} + k\gamma) + h(t - 2\Delta t, \phi_{mk}) + h(t - 3\Delta t, \phi_{mk})] \\
&\approx 4h'(t, \phi_{mk})\Delta t - 4h'(t, \phi_{mk} + k\gamma)\Delta t,
\end{aligned} \tag{37}$$

where Δt represents the laser propagation time from one satellite to another. It is evident that the ratio of Δt to L yields the speed of light, denoted as c . Therefore, we substitute the derivative of Eq. (34) into Eq. (37), replacing Δt and L with c . Finally, we obtain the result that describes the response generated by Earth's free oscillations in the TDI-X channel for TianQin. For convenience, we revert φ^{om} , which represents the argument of latitude of the midpoint of SC1 and SC2, back to φ^o , which represents the argument of latitude of SC1. Subsequently, we present the final result as

$$\begin{aligned}
h_X(t) &= \sum_{l=0}^L \sum_{n=0}^N \sum_{m=0}^n \sum_{k=-n[2]}^n \exp[-{}_l \lambda_{mn}(t - t_0)] \sum_{k=-n[2]}^n \frac{1}{2} \Xi_{mnk}(a, i, \gamma) \times \\
&\quad [{}_l P_{nm}^{+c} \cos({}_l \omega_{mnk}^+ (t - t_0) + \phi_{mk}) + {}_l P_{nm}^{+s} \sin({}_l \omega_{mnk}^+ (t - t_0) + \phi_{mk}) \\
&\quad + {}_l P_{nm}^{-c} \cos({}_l \omega_{mnk}^- (t - t_0) - \phi_{mk}) + {}_l P_{nm}^{-s} \sin({}_l \omega_{mnk}^- (t - t_0) - \phi_{mk})],
\end{aligned} \tag{38}$$

where

$$\begin{aligned}
{}_lP_{mnk}^{+c} &= \frac{8}{c} \cdot \sin\left(\frac{k\gamma}{2}\right) \cdot \frac{1}{(l\lambda_n)^2 + (l\omega_{mnk}^+)^2} (\omega_{mnk}^+ l \Delta\alpha_{nm} + l\lambda_{nl} \Delta\beta_{nm}) \\
{}_lP_{mnk}^{+s} &= \frac{8}{c} \cdot \sin\left(\frac{k\gamma}{2}\right) \cdot \frac{1}{(l\lambda_n)^2 + (l\omega_{mnk}^+)^2} (-\omega_{mnk}^+ l \Delta\beta_{nm} + l\lambda_{nl} \Delta\alpha_{nm}) \\
{}_lP_{mnk}^{-c} &= -\frac{8}{c} \cdot \sin\left(\frac{k\gamma}{2}\right) \cdot \frac{1}{(l\lambda_n)^2 + (l\omega_{mnk}^-)^2} (\omega_{mnk}^- l \Delta\alpha_{nm} - l\lambda_{nl} \Delta\beta_{nm}) \\
{}_lP_{mnk}^{-s} &= -\frac{8}{c} \cdot \sin\left(\frac{k\gamma}{2}\right) \cdot \frac{1}{(l\lambda_n)^2 + (l\omega_{mnk}^-)^2} (\omega_{mnk}^- l \Delta\beta_{nm} + l\lambda_{nl} \Delta\alpha_{nm}).
\end{aligned} \tag{39}$$

2.4 Parameter estimation method

The parameters of Earth's free oscillations can be estimated using TianQin observed data and the analytical model derived above. The frequencies and attenuation factors of various oscillation modes can be calculated using the PREM model [2], which is verified by ground experiments. Meanwhile, the coefficients of intensities ${}_l\Delta\bar{C}_{nm}$ and ${}_l\Delta\bar{S}_{nm}$ depend on the physical processes of earthquakes [41–43]. Therefore, we fix the frequencies and the attenuation factors of oscillation modes and estimate the coefficients of intensities to provide information for earthquake and related studies.

In this study, we adopt the Bayesian framework to obtain the posterior distribution of the parameters Θ and to provide parameter estimation results and precision based on the posterior. Bayesian theorem states that the posterior can be expressed as

$$p(\Theta|d, I) = \frac{p(d|\Theta, I)p(\Theta|I)}{p(d|I)}, \tag{40}$$

where $p(\Theta|d, I)$, $p(d|\Theta, I)$, $p(\Theta|I)$ and $p(d|I)$ represent the posterior, the likelihood, the prior and the normalization factor, respectively. The symbol I represents the information about signal and noise.

For the TianQin mission, we usually assume that the noise in the detector is Gaussian and stationary, so the likelihood could be expressed as

$$\begin{aligned}
\log \mathcal{L}(\Theta) &= \log p(d|\Theta, I) \\
&= -\frac{1}{2} \langle d - h(\Theta) | d - h(\Theta) \rangle + \text{const.} \\
&= \langle d | h(\Theta) \rangle - \frac{1}{2} \langle h(\Theta) | h(\Theta) \rangle - \frac{1}{2} \langle d | d \rangle + \text{const.},
\end{aligned} \tag{41}$$

where $h(\Theta)$ denotes the waveform which we derive in the Section 2.3. The symbol $\langle g | h \rangle$ represents the inner product between g and h

$$\langle g | h \rangle = 4\mathcal{R} \int_0^\infty \frac{\tilde{g}(f) \cdot \tilde{h}^*(f)}{S_n(f)} df, \tag{42}$$

where $S_n(f)$ denotes the one-side power spectral density (PSD) of the noise, and \mathcal{R} represents the real component.

The constant terms in the likelihood can be absorbed into the normalization factor, rendering

them negligible in our method for posterior calculation. Consequently, the likelihood simplifies to

$$\mathcal{L}(\Theta) \propto \exp \left[\langle d | h(\Theta) \rangle - \frac{1}{2} \langle h(\Theta) | h(\Theta) \rangle \right]. \quad (43)$$

Within the Bayesian framework, the prior represents the information or knowledge prior to starting the analysis. In our study, as we do not incorporate information from other observations, we assume a uniform distribution for the prior. Subsequently, we proceed to calculate the posterior.

The Earth's free oscillations generated by a major earthquake, as analyzed in this study, contain up to eight observable modes for TianQin. These modes contain 15 parameters. Consequently, we must analyze a high-dimensional parameter space for posterior calculation. Stochastic sampling methods, such as MCMC, are commonly employed to efficiently explore the parameter space. The MCMC method uses random walkers to generate samples, with a focus on moving towards regions of high posterior probability. In this study, we employ **emcee**, an ensemble sampling MCMC algorithm, for posterior distribution sampling [47]. Subsequently, upon obtaining posterior distribution samples, properties of the source parameters like their means and variance can be derived (Fig. 3 and 4).

However, since the MCMC algorithm involves randomness during sampling, it is necessary to validate its estimation results using alternative methods. In this study, the FIM method is utilized for validation [48–50]. While estimating the parameters of GWs, the FIM can be defined as

$$\Gamma_{ij} = \left\langle \frac{\partial h}{\partial \theta^i} \middle| \frac{\partial h}{\partial \theta^j} \right\rangle. \quad (44)$$

Subsequently, the covariance matrix between all parameters can be approximated as $\Sigma = \Gamma^{-1}$. Therefore, the estimation error can be estimated by

$$\delta\theta^i = \sqrt{\Sigma^{ii}}. \quad (45)$$

Comparing these results with the results obtained utilizing the MCMC method allows us to verify the accuracy of the MCMC parameter estimation.

3 Results

3.1 Analytical model verification

Prior to extracting Earth's free oscillation signals from TianQin simulation observation data, it is imperative to validate the efficacy of our analytical model. Observation data are generated employing both the analytical waveform and numerical simulation methods, utilizing identical parameters derived from a magnitude 7.9 earthquake. The resulting outputs from these divergent approaches are compared in Fig. 1. It is evident that, apart from a minor discrepancy near the occurrence of the earthquake, the outcomes yielded by these two models exhibit remarkable proximity, signifying the efficacy of our analytical waveform in accurately describing Earth's free oscillations in TianQin.

In Fig. 2, we also show our waveform in the frequency domain, comparing it with the designed

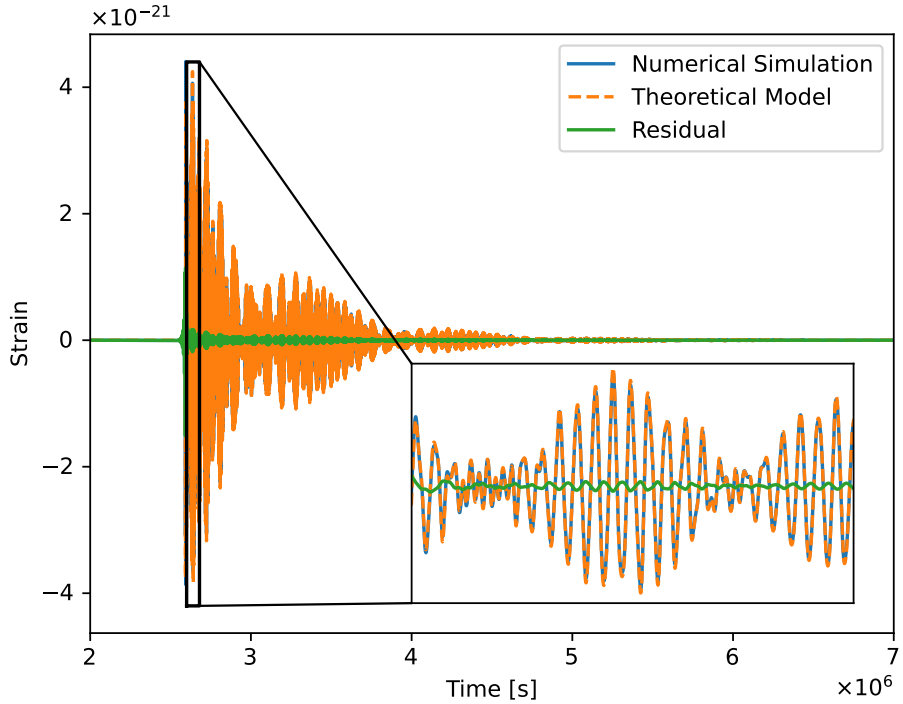


Figure 1: The figure illustrates the Earth's free oscillation response within the TianQin TDI-X channel, derived from both numerical simulation and analytical modeling approaches. The earthquake that induces the Earth's free oscillations occurs on day 30. The numerical simulation result is depicted by the blue solid line, while the analytical model result is represented by the orange dashed line. The green solid line illustrates the residual resulting from the subtraction of the aforementioned two results. With the exception of a minor region near the occurrence of the earthquake, the numerical result closely aligns with the predictions of the analytical formula.

noise for TianQin. Similar to the time domain result, the data are generated from the same magnitude 7.9 earthquake. The characteristic strain [51] in the frequency domain $h_c(f) = f|\tilde{h}(f)|$ is shown on top of the noise $h_n(f) = \sqrt{fS_n(f)}$, where $\tilde{h}(f)$ is the Fourier transform of the signal, and $S_n(f)$ represents the PSD of noise. One can define the SNR of a signal as $\rho^2 = 4 \int_0^\infty \frac{\tilde{h}^*(f)\tilde{h}(f)}{S_n(f)} df$. The SNR of the signal shown in Fig. 2 is 73, confirming previous studies on the detectability.

An important difference between space-based and ground-based detection can also be observed from Fig. 2: the frequencies of Earth's normal modes have split due to the rotation of both the Earth and the satellites. Our analytical waveform can predict the splitting frequency, which matches the simulation well. The way frequencies split depends on the spherical harmonic function basis. This allows us to directly estimate the different spherical harmonic amplitude of the Earth's normal modes, ${}_l\Delta\bar{C}_{nm}$ and ${}_l\Delta\bar{S}_{nm}$, using a single detector instead of joint detection with multiple detectors on the ground, which helps to avoid potential calibration errors among different detectors.

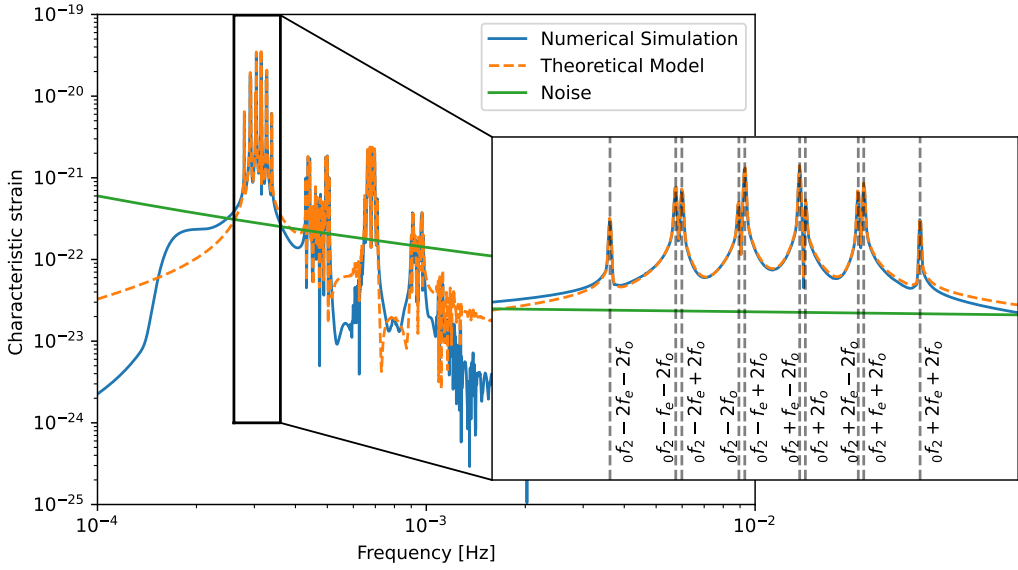


Figure 2: The figure illustrates the Earth’s free oscillations response within the TianQin TDI-X channel in the frequency domain. Both numerical simulation data (blue solid line) and analytical modeling data (orange dashed line) are plotted in this figure. In the zoomed-in plot, the spectrum of the ${}_0S_2$ mode is depicted. ${}_0f_2$, f_e and f_o denote frequencies of ${}_0S_2$ mode, Earth’s rotation, and satellites’ rotation respectively. It can be seen that this mode is split into 10 distinct spectral lines due to the influence of Earth’s and satellites’ rotation. Spectra splitting also occurs in other modes, and they can all be described by the analytical model (Eq. (32)–(38)). Different modes could add up deconstructive since they have opposite phases, making the overall peak appear to be slightly shifted. This is exactly what happens in certain frequencies like ${}_0f_2 - f_e + 2f_o$, ${}_0f_2 - f_e + 2f_o$, ${}_0f_2 + f_e - 2f_o$ and ${}_0f_2 + f_e + 2f_o$. The green line represents the noise amplitude of TianQin TDI-X channel [52].

3.2 Parameter estimation

In this section, we utilize the analytical waveform to extract signals from simulated observation data and estimate the parameters associated with Earth’s normal modes. The simulated observation data contains both numerical simulation signal from Earth’s free oscillations generated by the Wenchuan earthquake and the background noise generated from TDI-X channel theoretical PSD [31, 35, 52]. The frequencies and attenuation factors of the Earth’s free oscillations are held fixed, and we employ the MCMC method to sample the posterior distribution of the amplitude coefficients ${}_l\Delta\bar{C}_{nm}$ and ${}_l\Delta\bar{S}_{nm}$. Subsequently, we compute the means and variances of the sample set to obtain the estimates and accuracy. To verify the accuracy of the parameter estimation results, we compare them with those obtained using the FIM method [48–50]. For display purposes, we exclusively focus on the 9 modes with the highest response intensities, as the other high-order modes are submerged in background noise due to their weak response intensity.

The measured values of the parameters along with their errors are presented in Table 2. A more detailed and direct comparison can be made in Fig. 3, in which the violin plot is drawn for these parameters. To avoid the impact of discrepancies between the analytical waveform and numerical

Parameters	True values	Estimated values	FIM estimation errors
${}_0\Delta\bar{C}_{20}$	2.496×10^{-13}	$(2.39 \pm 0.20) \times 10^{-13}$	0.19×10^{-13}
${}_0\Delta\bar{S}_{20}$	0.0	-	-
${}_0\Delta\bar{C}_{21}$	1.086×10^{-12}	$(1.018 \pm 0.021) \times 10^{-12}$	0.020×10^{-12}
${}_0\Delta\bar{S}_{21}$	3.552×10^{-13}	$(4.02 \pm 0.22) \times 10^{-13}$	0.23×10^{-13}
${}_0\Delta\bar{C}_{22}$	7.799×10^{-13}	$(7.49 \pm 0.35) \times 10^{-13}$	0.34×10^{-13}
${}_0\Delta\bar{S}_{22}$	3.650×10^{-13}	$(4.13 \pm 0.35) \times 10^{-13}$	0.34×10^{-13}
${}_0\Delta\bar{C}_{32}$	-1.662×10^{-13}	$(-0.4 \pm 1.5) \times 10^{-13}$	1.4×10^{-13}
${}_0\Delta\bar{S}_{32}$	6.689×10^{-13}	$(4.0 \pm 1.5) \times 10^{-13}$	1.4×10^{-13}
${}_0\Delta\bar{C}_{33}$	-5.813×10^{-13}	$(-7.3 \pm 1.2) \times 10^{-13}$	1.2×10^{-13}
${}_0\Delta\bar{S}_{33}$	3.436×10^{-13}	$(3.7 \pm 1.2) \times 10^{-13}$	1.2×10^{-13}
${}_1\Delta\bar{C}_{20}$	2.369×10^{-13}	$(2.02 \pm 0.83) \times 10^{-13}$	0.60×10^{-13}
${}_1\Delta\bar{S}_{20}$	0.0	-	-
${}_1\Delta\bar{C}_{21}$	-2.957×10^{-13}	$(-3.37 \pm 0.58) \times 10^{-13}$	0.54×10^{-13}
${}_1\Delta\bar{S}_{21}$	3.537×10^{-13}	$(3.27 \pm 0.95) \times 10^{-13}$	0.77×10^{-13}
${}_1\Delta\bar{C}_{22}$	-3.762×10^{-13}	$(-2.5 \pm 1.1) \times 10^{-13}$	0.73×10^{-13}
${}_1\Delta\bar{S}_{22}$	-4.451×10^{-13}	$(-5.55 \pm 0.92) \times 10^{-13}$	0.82×10^{-13}
${}_1\Delta\bar{C}_{33}$	5.431×10^{-13}	$(15.1 \pm 3.2) \times 10^{-13}$	2.6×10^{-13}
${}_1\Delta\bar{S}_{33}$	-2.053×10^{-13}	$(-10.2 \pm 3.1) \times 10^{-13}$	2.4×10^{-13}

Table 2: Corrections to the geopotential coefficients due to the earthquake and the estimated values. The last column shows the parameter estimation error obtained based on FIM, validating the accuracy of the parameter estimation results obtained by the MCMC method.

simulation results near the occurrence of the earthquake, only the data from 5 hours to 15 days after the earthquake is applied for parameter estimation.

4 Discussion

This study introduces a novel approach to detecting Earth's free oscillations utilizing TianQin. Unlike other space gravity measurement missions such as GRACE [24] and TianQin-2 [28], TianQin's satellites operate in high Earth orbit, mitigating the influence of Earth's high-order gravity field and facilitating the maintenance of quasi-circular orbits. Crucially, the three assumptions – quasi-circular orbits, equal orbital altitude, and an equilateral triangle constellation for the three satellites – are fundamental for deriving analytical waveforms to characterize Earth's free oscillations in TianQin. These assumptions allow the modulation effects of satellite motion on signals of Earth's free oscillations to be described using a single constant, the satellite orbital frequency, thereby neglecting high-order effects. They also simplify the calculation for TDI channel. Through a comparison with numerical simulation data in both the time domain and frequency domain, we observe a noteworthy concordance between the analytical waveform and the simulation data, affirming the efficacy of the analytical approach in capturing the response arising from Earth's free oscillations in TianQin. The ability to formulate an analytical waveform for Earth's free oscillations represents a significant advantage afforded by high-orbit satellites, enabling the extraction of information from observation data beyond just observation.

Through the MCMC method, we demonstrate that it is possible to extract physical information

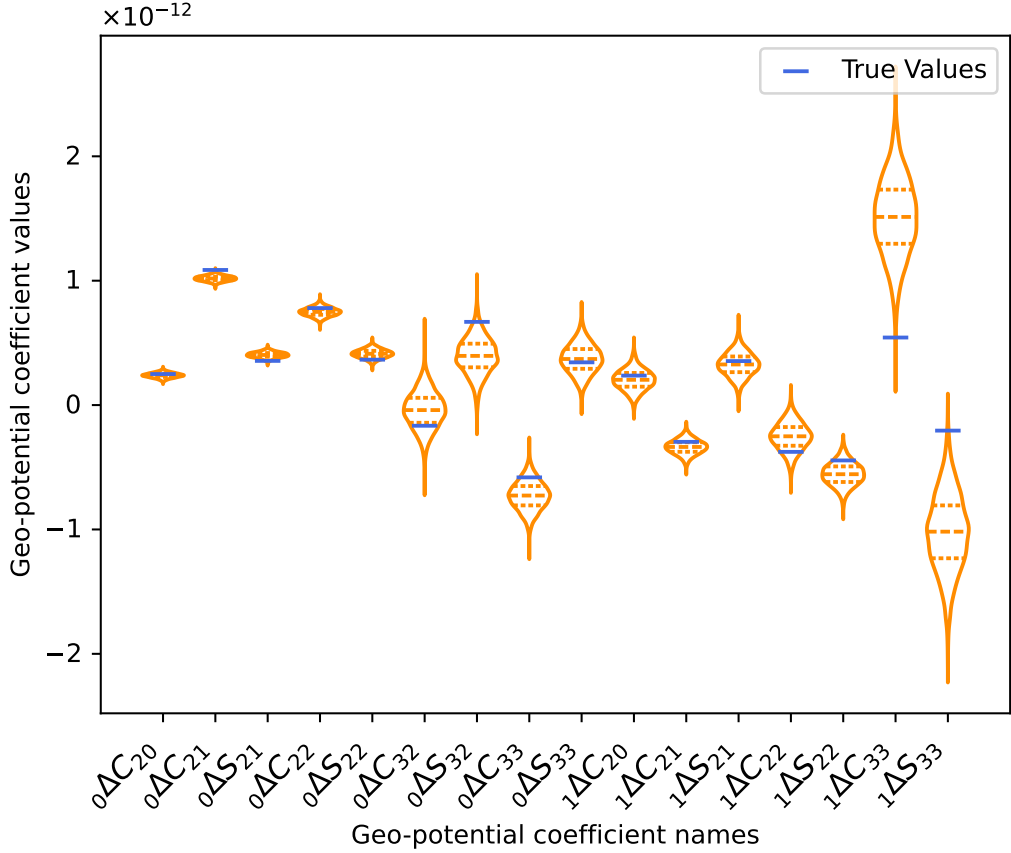


Figure 3: This figure shows the parameter estimation results and accuracy. The blue lines mark the true values we use to generate simulation data.

about the Earth's free oscillation from TianQin's observation data. For the injected signal caused by the Wenchuan-like earthquake, TianQin is capable of detecting approximately 9 modes. This result suggests that the GW observatory, TianQin, can open a new window to examine the Earth's normal modes. Compared to the ground-based stations, the satellite gravity method has a different source of noise, which can provide precious independent cross-validation. Additionally, as shown in Eq. 12, some of Earth's normal modes are frequency degeneracy, necessitating joint detection with multiple detectors for ground-based stations to distinguish them, which introduces potential calibration errors among different detectors. The scanning effect of satellites can split these frequencies as Fig. 2 shown, thus breaking this degeneracy. This allows TianQin to distinguish different modes independently, which can effectively avoid calibration errors.

The primary goal of the TianQin mission is to detect GWs. Earth's free oscillation signals and GW signal may occur simultaneously on a rare occasion. Due to the significant difference between the waveforms of these two kinds of signals, they are in principle unlikely to be confused. When both signals are present in the observed data, a global analysis method can be employed to separate them [53]. However, the details of method strategies require further investigation in the future.

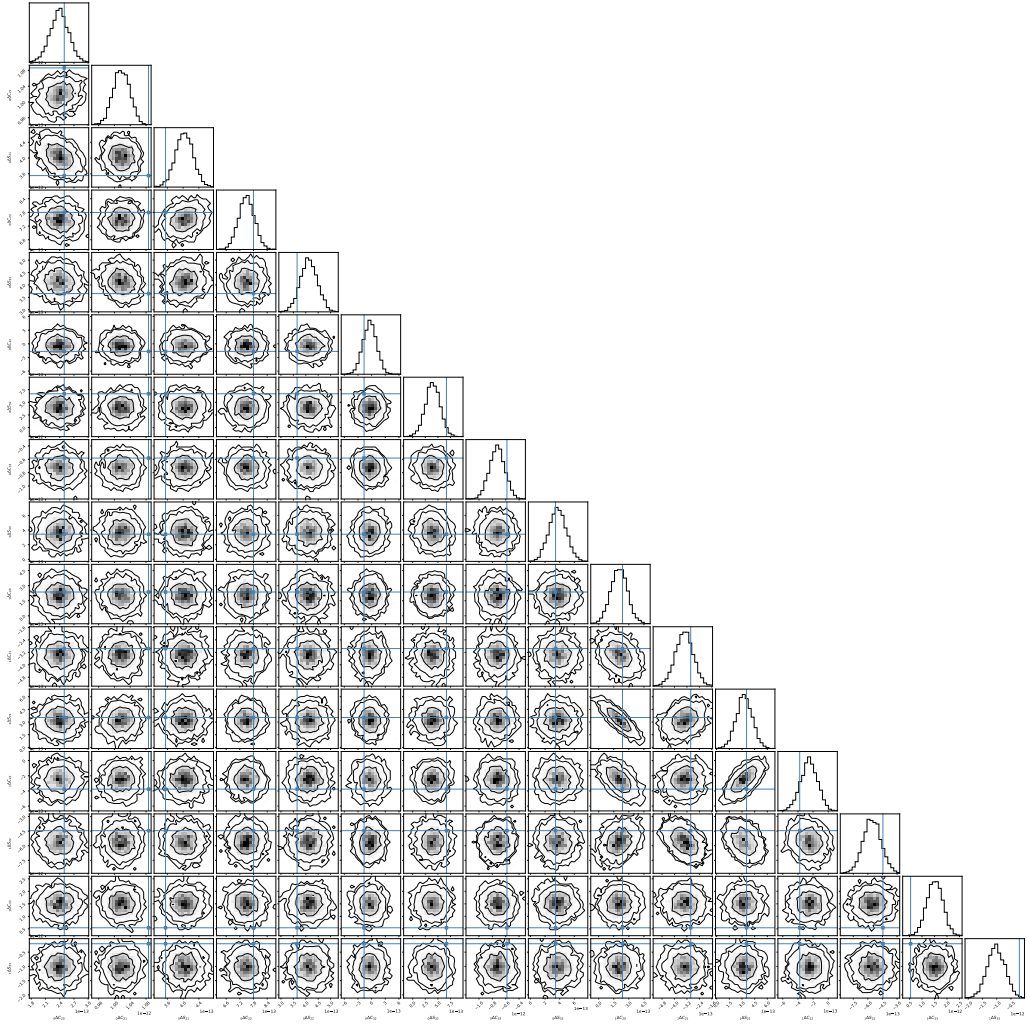


Figure 4: The corner plots show the two-dimensional posterior distribution between different parameters. The blue lines show the injected values of parameters in simulated data.

Our analysis in this study focuses on the data in the TDI-X channel. The symmetry of the TDI method [35] allows for the straightforward generalization of our analytical waveform to the TDI-Y or TDI-Z channels by adjusting the phase of the satellite's orbit. In the field of space GW detection, there is another widely used TDI channel known as the AET channel [36]. Unlike the XYZ channel, this channel consists of three orthogonal channels, with GW signals concentrated in the A and E channels, while the T channel primarily reflects detector noise. Additionally, we conducted analyses using the AET channel. Our findings suggest that our reconstructed waveform can effectively describe the response signals observed in both the TDI-A and TDI-E channels. Unlike the GW signals, numerical simulated data reveals high SNR responses of Earth's free oscillations in the TDI-T channel. The reason for the different phenomena of Earth gravity perturbations and astrophysical-origin gravity perturbations in the TDI-T channel lies in the assumption that GWs

can be approximated as plane waves, which holds true for the latter but fails for the former. Similar to the result in [54], the effectiveness of the plane wave assumption changes the way GWs respond, suggesting that the T channel no longer primarily reflects noise. Unfortunately, the theoretical waveforms we currently derive cannot adequately describe the response of Earth’s free oscillations in the TDI-T channel. We plan to develop more sophisticated models to describe this response in the future, which will help separate the signals when TianQin observes both GWs and major earthquakes at the same time.

Acknowledgments

General

We thank Khosro Ghobadi-Far for providing helpful materials on GRACE’s detection of Earth’s free oscillations. We thank Chengjian Luo and Lu Zheng for their support and assistance in generating numerical simulation data. We thank Lei Jiao for his assistance with deriving the formulas. We also thank Rongjiang Wang, Yong Zhang, Xiang’e Lei, Hao Zhou, Hang Li, Jiandong Zhang, Enkun Li, Zhengcheng Liang, and Zhiyuan Li for their helpful discussions and comments.

Author Contributions

Yi-Ming Hu and Xuefeng Zhang designed the research. Yuxin Yang derived the formulas in this research. Yuxin Yang and Kun Liu analyzed the data. Yuxin Yang, Kun Liu, Xuefeng Zhang, and Yi-Ming Hu wrote the paper.

Funding

X. Z. is supported by the National Key R&D Program of China (Grant Nos. 2020YFC2201202 and 2022YFC2204600), NSFC (Grant No. 12373116), and Fundamental Research Funds for the Central Universities, Sun Yat-sen University (Grant No. 23xkjc001). Y. H. is supported by the National Key Research and Development Program of China (No. 2020YFC2201400), the Natural Science Foundation of China (Grants No. 12173104, No. 12261131504), and Guangdong Major Project of Basic and Applied Basic Research (Grant No. 2019B030302001).

Conflicts of Interest

The authors declare that they have no conflict of interest.

Data Availability

All data needed to evaluate the conclusions in the paper are present in the paper and/or the Supplementary Materials. Additional data related to this paper may be requested from the authors

Supplementary Materials

No additional supplementary materials were provided.

References

1. Dziewonski AM. Overtones of free oscillations and the structure of the Earth's interior. *Science* 1971;172:1336–8.
2. Dziewonski AM and Anderson DL. Preliminary reference Earth model. *Physics of the Earth and Planetary Interiors* 1981;297–356.
3. Dziewonski A and Gilbert F. Solidity of the inner core of the Earth inferred from normal mode observations. *Nature* 1971;234:465–6.
4. Woodhouse JH, Giardini D, and Li XD. Evidence for inner core anisotropy from free oscillations. *Geophysical Research Letters* 1986;13:1549–52.
5. Tromp J. Support for anisotropy of the Earth's inner core from free oscillations. *Nature* 1993;366:678–81.
6. Romanowicz B and Bréger L. Anomalous splitting of free oscillations: A reevaluation of possible interpretations. *Journal of Geophysical Research: Solid Earth* 2000;105:21559–78.
7. Masters G, Jordan TH, Silver PG, and Gilbert F. Aspherical Earth structure from fundamental spheroidal-mode data. *Nature* 1982;298:609–13.
8. Ishii M and Tromp J. Normal-mode and free-air gravity constraints on lateral variations in velocity and density of Earth's mantle. *Science* 1999;285:1231–6.
9. Gilbert F and Dziewonski A. An application of normal mode theory to the retrieval of structural parameters and source mechanisms from seismic spectra. *Philosophical Transactions of the Royal Society of London. Series A, Mathematical and Physical Sciences* 1975;278:187–269.
10. Ritzwoller MH and Lavelle EM. Three-dimensional seismic models of the Earth's mantle. *Reviews of Geophysics* 1995;33:1–66.
11. Park J, Song TRA, Tromp J, et al. Earth's free oscillations excited by the 26 December 2004 Sumatra-Andaman earthquake. *Science* 2005;308:1139–44.
12. Ness N, Harrison J, and Slichter L. Observations of the free oscillations of the earth. *Journal of Geophysical Research* 1961;66:621–9.
13. Benioff H, Press F, and Smith S. Excitation of the free oscillations of the Earth by earthquakes. *Journal of Geophysical Research* 1961;66:605–19.
14. Dziewonski A and Gilbert F. Observations of normal modes from 84 recordings of the Alaskan earthquake of 1964 March 28. *Geophysical Journal International* 1972;27:393–446.
15. Geller RJ and Stein S. Time-domain attenuation measurements for fundamental spheroidal modes (${}_0S_6$ to ${}_0S_{28}$) for the 1977 Indonesian earthquake. *Bulletin of the Seismological Society of America* 1979;69:1671–91.

16. Ding H and Chao BF. Data stacking methods for isolation of normal-mode singlets of Earth's free oscillation: Extensions, comparisons, and applications. *Journal of Geophysical Research: Solid Earth* 2015;120:5034–50.
17. Buland R, Berger J, and Gilbert F. Observations from the IDA network of attenuation and splitting during a recent earthquake. *Nature* 1979;277:358–62.
18. Ding H and Shen WB. Search for the Slichter modes based on a new method: Optimal sequence estimation. *Journal of Geophysical Research: Solid Earth* 2013;118:5018–29.
19. Courtier N, Ducarme B, Goodkind J, et al. Global superconducting gravimeter observations and the search for the translational modes of the inner core. *Physics of the Earth and Planetary Interiors* 2000;117:3–20.
20. Rosat S, Sato T, Imanishi Y, et al. High-resolution analysis of the gravest seismic normal modes after the 2004 $M_w = 9$ Sumatra earthquake using superconducting gravimeter data. *Geophysical research letters* 2005;32.
21. Rosat S, Hinderer J, and Rivera L. First observation of 2S1 and study of the splitting of the football mode 0S2 after the June 2001 Peru earthquake of magnitude 8.4. *Geophysical Research Letters* 2003;30.
22. Deuss A, Ritsema J, and Heijst H van. A new catalogue of normal-mode splitting function measurements up to 10 mHz. *Geophysical Journal International* 2013;193:920–37.
23. Luan W, Shen W, and Ding H. Progress and prospect of studies on elastic normal modes of Earth's free oscillation. *Reviews of Geophysics and Planetary Physics* 2021;52:308–25.
24. Ghobadi-Far K, Han SC, Sauber J, et al. Gravitational Changes of the Earth's Free Oscillation From Earthquakes: Theory and Feasibility Study Using GRACE Inter-satellite Tracking. *Journal of Geophysical Research: Solid Earth* 2019;124:7483–503.
25. Tapley BD, Bettadpur S, Watkins M, and Reigber C. The gravity recovery and climate experiment: Mission overview and early results. *Geophysical Research Letters* 2004;n/a–n/a.
26. Kornfeld RP, Arnold BW, Gross MA, et al. GRACE-FO: The Gravity Recovery and Climate Experiment Follow-On Mission. *Journal of Spacecraft and Rockets* 2019;56:931–51.
27. Mei J, Bai YZ, Bao J, et al. The TianQin project: Current progress on science and technology. *Progress of Theoretical and Experimental Physics* 2020;2021:05A107.
28. Gong Y, Luo J, and Wang B. Concepts and status of Chinese space gravitational wave detection projects. *Nature Astronomy* 2021;5:881–9.
29. Abich K, Abramovici A, Amparan B, et al. In-Orbit Performance of the GRACE Follow-on Laser Ranging Interferometer. *Phys. Rev. Lett.* 3 2019;123:031101.
30. Liu K. Effects of Sun and Earth's free oscillations on TianQin's range acceleration noise. MA thesis. Sun Yat-sen University, 2023.
31. Luo J, Chen LS, Duan HZ, et al. TianQin: a space-borne gravitational wave detector. *Classical and Quantum Gravity* 2016;035010.

32. Zhang X, Luo C, Jiao L, et al. Effect of Earth-Moon's gravity on TianQin's range acceleration noise. *Physical Review D* 2021;103.
33. Jiao L and Zhang X. Effect of Earth-Moon's gravity on TianQin's range acceleration noise. III. An analytical model. *Phys. Rev. D* 2023;107:102004.
34. Christensen N and Meyer R. Parameter estimation with gravitational waves. *Reviews of modern physics* 2022;94:025001.
35. Tinto M and Armstrong JW. Cancellation of laser noise in an unequal-arm interferometer detector of gravitational radiation. *Physical Review D* 1999;59:102003.
36. Armstrong J, Estabrook F, and Tinto M. Time-delay interferometry for space-based gravitational wave searches. *The Astrophysical Journal* 1999;527:814.
37. Tinto M and Dhurandhar SV. Time-Delay Interferometry. *Living Reviews in Relativity* 2014.
38. Kaula WM. Analysis of Gravitational and Geometric Aspects of Geodetic Utilization of Satellites. *Geophysical Journal International* 1961;5:104–33.
39. Kaula WM. Theory of Satellite Geodesy. Blaisdell Publishing Company, 1966.
40. Woodhouse J, Deuss A, and Schubert G. Theory and observations—Earth's free oscillations. *Seismology and Structure of the Earth: Treatise on Geophysics* 2010;1:31.
41. Kanamori H and Cipar JJ. Focal process of the great Chilean earthquake May 22, 1960. *Physics of the Earth and Planetary Interiors* 1974;9:128–36.
42. Stein S and Geller RJ. Amplitudes of the Earth's split normal modes. *Journal of Physics of the Earth* 1977;25:117–42.
43. Stein S and Wysession M. An introduction to seismology, earthquakes, and earth structure. John Wiley & Sons, 2009.
44. Montenbruck O and Gill E. *Satellite Orbits - Models, Methods, and Applications*. Springer, 2000.
45. Han SC, Riva R, SauPer J, and Okal E. Source parameter inversion for recent great earthquakes from a decade-long observation of global gravity fields. *Journal of Geophysical Research: Solid Earth* 2013;118:1240–67.
46. Sharifi MA. Satellite to Satellite Tracking in the Space-wise Approach. Ph.D. thesis. University of Stuttgart, 2006.
47. Foreman-Mackey D, Hogg DW, Lang D, and Goodman J. emcee: The MCMC Hammer. *Publications of the Astronomical Society of the Pacific* 2013;306–12.
48. Cutler C and Flanagan EE. Gravitational waves from merging compact binaries: How accurately can one extract the binary's parameters from the inspiral waveform? *Physical Review D* 1994;49:2658.
49. Vallisneri M. Use and abuse of the Fisher information matrix in the assessment of gravitational-wave parameter-estimation prospects. *Physical Review D* 2008;77:042001.

50. Rodriguez CL, Farr B, Farr WM, and Mandel I. Inadequacies of the Fisher information matrix in gravitational-wave parameter estimation. *Physical Review D* 2013;88:084013.
51. Moore CJ, Cole RH, and Berry CPL. Gravitational-wave sensitivity curves. *Classical and Quantum Gravity* 2014;32:015014.
52. Li EK et al. GWSpace: a multi-mission science data simulator for space-based gravitational wave detection. 2023.
53. Littenberg TB and Cornish NJ. Prototype global analysis of LISA data with multiple source types. *Phys. Rev. D* 2023;107:063004.
54. Guo X, Lu Y, and Yu Q. On Detecting Nearby Nanohertz Gravitational Wave Sources via Pulsar Timing Arrays. *The Astrophysical Journal* 2022;939:55.